Interference of current distortion patterns and magnetoresistance anisotropy in a composite with periodic microstructure

Yakov M. Strelniker and David J. Bergman
School of Physics and Astronomy, Raymond and Beverly Sackler Faculty of Exact Sciences, Tel Aviv University, Tel Aviv 69978, Israel
(Received 28 June 1995; revised manuscript received 5 December 1995)

A detailed theoretical and numerical study is presented of the anisotropic magnetotransport which was recently predicted to occur in composite conductors with a periodic microstructure. Contour plots and three-dimensional graphs of the local dissipation rate around an isolated obstacle and around a periodic array of obstacles, as well as vector plots of the distorted current pattern, are produced and used to discuss the details of the anisotropic magnetoresistance. The problem of an isolated spherical or cylindrical inclusion in a homogeneous host has a closed form solution. This is exploited in order to give a perturbation treatment of the problem of multiple inclusions. A good qualitative understanding of many features of the anisotropy can be achieved by considering the interference between the current distortion patterns produced by just two obstacles of either spherical or cylindrical shape. As a result of these discussions, we have now achieved a more complete understanding of how the anisotropic magnetotransport arises in a periodic composite conductor.

I. INTRODUCTION

The strong field magnetoresistance of a composite medium with a *periodic microstructure* was recently predicted by us to exhibit a strong dependence on the precise orientations of the external magnetic field **H** and the volume averaged current density $\langle \mathbf{J} \rangle$, very similar to its behavior in certain metallic single crystals (see Fig. 14 in Ref. 1). This effect has yet to be verified experimentally. Unfortunately, measurements of magnetotransport in composite conductors are quite rare and until now were confined to disordered composite media,[2,3] as were also most of the theoretical discussions.[4–17] This is related to the fact that periodic composite media are not commonplace: although three-dimensional (3D) periodic *dielectric* composites are now used in order to achieve photonic band gap environments,[18] 3D periodic *conducting* composites have not yet been fabricated, as far as we know. However, it may be possible to produce such materials by applying heavy doses of radiation to a metallic crystal—these sometimes lead to the formation of mesoscopic cavities, or other defect clusters, which have a tendency to form periodic arrays.[19–23] Also, in order to observe the effects predicted in Ref. 1, at least one component must have a large electron mobility in order to achieve a large value of the dimensionless magnetic field H, which is actually equal to the Hall-to-Ohmic resistivity ratio. It seems to us that the only system on which the necessary experiments could be carried out now is a thin film with a two-dimensional (2D) periodic array of inhomogeneities. Such systems can be conveniently fabricated using the same microlithographic techniques which are used to fabricate arrays of quantum dots and antidots.[24–34] The extension of the theory, previously developed for 3D systems, to thin films is discussed in Ref. 35.

The theoretical and numerical results reported in Ref. 1 were obtained for a composite conductor with a periodic microstructure, namely, a simple cubic array of spheres or cylinders embedded in an isotropic conducting host medium which was taken to be a free-electron metal without any intrinsic magnetoresistance. The inclusions were either insulating or else conductors which are also of the free-electron-metal type, but with a different value of the resistivity than that of the host medium. The strong dependence of the bulk effective Ohmic resistivities upon **H** was explained by invoking a simple geometric shadow picture in order to discuss the interaction between the current distortions produced by neighboring inclusions. These distortions are entirely classical in nature, and they are found by solving the steady state current conservation or continuity equation $\nabla \cdot \mathbf{J} = 0$. Quantum mechanics seems to play no role in producing this behavior: not only are concepts like Fermi surface unnecessary, but even the very existence of discrete charge carriers is irrelevant. This is in marked contrast with the anisotropic magnetoresistance observed in single crystals of many transition metals, which could only be explained by considerations based upon the detailed shapes of the extended Fermi surfaces.[36–38] However, using the simple geometric shadow picture we were only able to explain some of the anisotropic features that emerged from the numerical calculations. In particular, one of the transverse components of the magnetoresistivity tensor exhibited behavior that was totally mysterious and remained unexplained.

In this article we report on attempts to improve our understanding of the above described phenomena by calculating the detailed distortion patterns of the local electric current density or flux $\mathbf{J}(\mathbf{r})$. This is done for isolated obstacles using closed form solutions which are obtainable in some cases when the obstacle has a simple shape. A simple superposition approximation is then used to discuss the interference between the distortion patterns of two neighboring obstacles. The current distortion pattern for a periodic array of spherical obstacles is also worked out using numerical methods.

The rest of this article is organized as follows. In Sec. II

we summarize the techniques used to evaluate the current distortions in the case of an isolated inclusion and in the case of a periodic array of inclusions. In Sec. III we consider the distortions in the dissipation pattern caused by a single obstacle and by an array of obstacles, as obtained from detailed calculations. In Sec. IV we consider the interference between distortion patterns of two neighboring obstacles in order to achieve a qualitative physical understanding of the behavior of the macroscopic bulk effective resistivity tensor, including the above mentioned mystery. Section V provides a discussion of these results.

II. SHORT DESCRIPTION OF THE CALCULATIONAL METHODS

We consider a nonhomogeneous medium that can be described as either a single inclusion, or else an array of inclusions, with a conductivity tensor $\hat{\sigma}_1$, embedded in a host material $\hat{\sigma}_2$. Such a system can be described by a position-dependent conductivity tensor $\hat{\sigma}(\mathbf{r})$,

$$\hat{\sigma}(\mathbf{r}) \equiv \hat{\sigma}_1 \theta_1(\mathbf{r}) + \hat{\sigma}_2 \theta_2(\mathbf{r}) = \hat{\sigma}_2 - \delta\hat{\sigma}\,\theta_1(\mathbf{r}), \tag{2.1}$$

$$\delta\hat{\sigma} \equiv \hat{\sigma}_2 - \hat{\sigma}_1, \tag{2.2}$$

where $\theta_1(\mathbf{r})$ is the characteristic or indicator function, equal to 1 for $\mathbf{r}$ inside the inclusions and 0 elsewhere. Similarly, $\theta_2(\mathbf{r})$ refers to the host material, so that $\theta_2(\mathbf{r}) = 1 - \theta_1(\mathbf{r})$. The conductivity $\hat{\sigma}(\mathbf{r})$ is thus a function of the microgeometry and the physical properties of each component. The current density is related to the electric potential $\phi(\mathbf{r})$ by Ohm's law $\mathbf{J}(\mathbf{r}) = \hat{\sigma}(\mathbf{r}) \cdot \nabla\phi(\mathbf{r})$, and it satisfies the current conservation condition,

$$\nabla \cdot [\hat{\sigma}(\mathbf{r}) \cdot \nabla\phi(\mathbf{r})] = 0. \tag{2.3}$$

This equation, if satisfied everywhere, also ensures that the appropriate continuity conditions are satisfied at the $\hat{\sigma}_1, \hat{\sigma}_2$ interface. Those conditions involve all elements of the conductivity tensor, i.e., the Ohmic conductivities as well as the Hall conductivity. By contrast, away from the interface the Hall conductivity drops out of the differential equation (2.3), since it corresponds to a constant antisymmetric part of $\hat{\sigma}(\mathbf{r})$.

A. Single inclusion

The problem of a single spherical inclusion with conductivity $\hat{\sigma}_1$, embedded in an otherwise uniform host medium with conductivity $\hat{\sigma}_2$, is a classical undergraduate exercise in the case where $\hat{\sigma}_1$, $\hat{\sigma}_2$ are both *scalar tensors*. The problem remains solvable even if the inclusion is an ellipsoid, and even if $\hat{\sigma}_1$, $\hat{\sigma}_2$ are nonscalar, nonsymmetric tensors. But in this general case the solution is quite complicated.[5] Here we restrict our discussion to an inclusion shape that is either a sphere or a circular cylinder, and to $\hat{\sigma}_1$, $\hat{\sigma}_2$ which are both of the free-electron-metal type and have the same Hall-to-Ohmic resistivity ratio $H \equiv \rho_{\mathrm{Hall}}/\rho_{\mathrm{Ohm}}$

$$\hat{\sigma}_i = \sigma_i \begin{pmatrix} \gamma & H\gamma & 0 \\ -H\gamma & \gamma & 0 \\ 0 & 0 & 1 \end{pmatrix}, \quad i = 1,2, \tag{2.4}$$

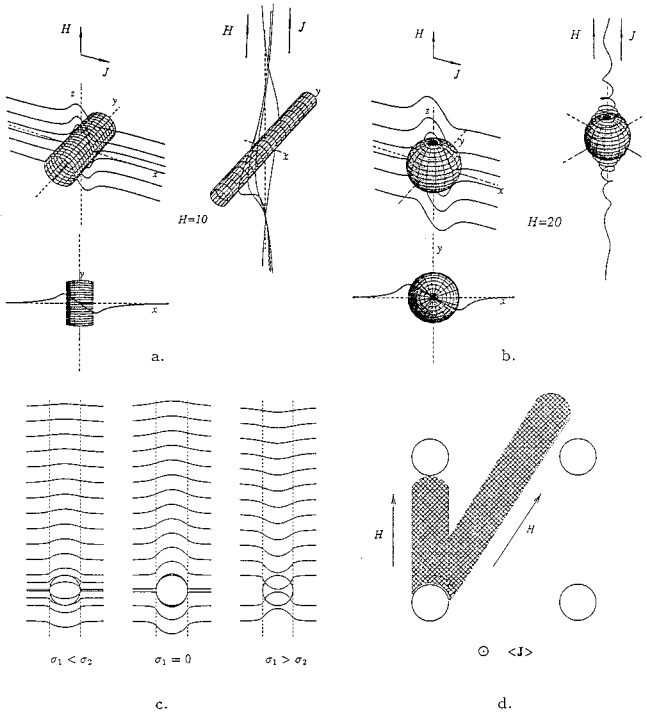

FIG. 1. (a) Isometric projections of current lines near a cylindrical obstacle ($\sigma_1 = 0$) for the case where $\mathbf{J}_0$ is injected perpendicular to $\mathbf{H}$ (top left) and for the case where $\mathbf{J}_0$ is parallel to $\mathbf{H}$ (top right) (after Ref. 39). At the bottom we show the first case ($\mathbf{J}_0 \perp \mathbf{H}$) as viewed from above, i.e., in the direction of $\mathbf{H}$. (b) Isometric projections of current lines near a spherical obstacle ($\sigma_1 = 0$) for the case where $\mathbf{J}_0$ is injected perpendicular to $\mathbf{H}$ (top left) and for the case where $\mathbf{J}_0$ is parallel to $\mathbf{H}$ (top right). At the bottom we again show the first case ($\mathbf{J}_0 \perp \mathbf{H}$) as viewed from above. (c) Projection on the x,z plane of the family of current lines near a cylindrical inclusion. Three cases are shown: $\sigma_1 < \sigma_2$, $\sigma_1 = 0$, and $\sigma_1 > \sigma_2$ (namely, $\sigma_1 = 0.5$, 0, and 2, while $\sigma_2 = 1$ in all cases). For a spherical inclusion the picture would be quite similar. The dashed lines indicate regions of high current density. (d) Schematic illustration showing how the onset of interference between the cylinders of current distortion from different inclusions depends on the orientation of the magnetic field with respect to the lattice of inclusions. The cross hatched strips indicate regions of high current distortion; the average current density $\langle \mathbf{J} \rangle$ is perpendicular to the plane of the figure.

$$\gamma \equiv (1 + H^2)^{-1}. \tag{2.5}$$

In Ref. 39 the explicit solution was worked out for the different possible magnetic field configurations in the case where the inclusion is a perfect insulator (i.e., $\sigma_1 = 0$). We have applied a similar analysis to the case where σ_1 and σ_2 are both nonzero. These solutions were used to produce Figs. 1(a) and 1(b), where some current flow lines are shown to indicate the nature of the distortions caused by an insulating inclusion. In Fig. 1(c) we show a planar projection of some of the distorted current flow lines around a cylindrical inclusion when its conductivity σ_1 is either smaller or greater than the host conductivity σ_2 (here $\langle \mathbf{J} \rangle \perp \mathbf{H}$ and both are perpendicular to the cylinder axis). In Fig. 1(d) we indicate how the region of strong current distortion extends from the in-

clusion in the direction of **H**, having approximately the shape of a long wall or cylinder with a cross section determined by the inclusion.

B. Multiple inclusions

When there is more than one inclusion, a closed form solution does not exist. We therefore use the approach of Ref. 40 in order to numerically evaluate the detailed form of the local electric potential $\phi(\mathbf{r})$.

In that approach, (2.3) is first transformed into an integro-differential equation, using Green's function $G(\mathbf{r},\mathbf{r}'|\hat{\boldsymbol{\sigma}}_2)$ for the uniform host medium:

$$\nabla\cdot\hat{\boldsymbol{\sigma}}_2\cdot\nabla G(\mathbf{r},\mathbf{r}'|\hat{\boldsymbol{\sigma}}_2)=-\delta^3(\mathbf{r}-\mathbf{r}'),$$
$$G=0 \text{ at the external boundaries,} \tag{2.6}$$

$$\phi^{(\alpha)}=r_\alpha+\hat{\Gamma}\phi^{(\alpha)}, \tag{2.7}$$

$$\hat{\Gamma}\phi\equiv\int dV'\,\theta_1(\mathbf{r}')\nabla' G(\mathbf{r},\mathbf{r}'|\hat{\boldsymbol{\sigma}}_2)\cdot\delta\hat{\boldsymbol{\sigma}}\cdot\nabla'\phi(\mathbf{r}'), \tag{2.8}$$

where $\phi^{(\alpha)}(\mathbf{r})$ is the local potential when the volume averaged field is a unit vector in the direction α,

$$\langle\nabla\phi^{(\alpha)}\rangle=\mathbf{e}_\alpha, \tag{2.9}$$

and $r_\alpha=(\mathbf{r}\cdot\mathbf{e}_\alpha)$. Note that G actually depends only on the symmetric part of $\hat{\sigma}_2$, denoted by $\hat{\sigma}_{2s}$.

If the microstructure is *periodic*, then both $\theta_1(\mathbf{r})$ and $\psi^{(\alpha)}(\mathbf{r})\equiv\phi^{(\alpha)}(\mathbf{r})-r_\alpha$ are *periodic functions*. Thus they can be expanded in appropriate Fourier series,

$$\psi^{(\alpha)}(\mathbf{r})=\sum_{\mathbf{g}}\psi_{\mathbf{g}}^{(\alpha)}e^{i\mathbf{g}\cdot\mathbf{r}},$$

$$\theta_1(\mathbf{r})=\sum_{\mathbf{g}}\theta_{\mathbf{g}}e^{i\mathbf{g}\cdot\mathbf{r}}.$$

Equation (2.7) is thereby transformed into an infinite system of linear algebraic equations for the expansion coefficients $\psi_{\mathbf{g}}^{(\alpha)}$, which are represented by

$$a_{\mathbf{g}}^{(\alpha)}\equiv i(\mathbf{g}\cdot\hat{\sigma}_{2s}\cdot\mathbf{g})^{1/2}\psi_{\mathbf{g}}^{(\alpha)} \quad \text{for } \mathbf{g}\neq 0, \tag{2.10}$$

namely (note that we use the summation convention for repeated vectorial or tensorial indices),

$$a_{\mathbf{g}}^{(\alpha)}=r_{\mathbf{g}}^{(\alpha)}+\sum_{\mathbf{g}'\neq 0}\Gamma_{\mathbf{g}\mathbf{g}'}a_{\mathbf{g}'}^{(\alpha)} \quad \text{for } \mathbf{g}\neq 0, \tag{2.11}$$

$$r_{\mathbf{g}}^{(\alpha)}\equiv\frac{g_\beta\delta\sigma_{\beta\alpha}\theta_{\mathbf{g}}}{(\mathbf{g}\cdot\hat{\sigma}_{2s}\cdot\mathbf{g})^{1/2}}, \tag{2.12}$$

$$\Gamma_{\mathbf{g}\mathbf{g}'}\equiv\frac{(\mathbf{g}\cdot\delta\hat{\sigma}\cdot\mathbf{g}')\,\theta_{\mathbf{g}-\mathbf{g}'}}{(\mathbf{g}\cdot\hat{\sigma}_{2s}\cdot\mathbf{g})^{1/2}(\mathbf{g}'\cdot\hat{\sigma}_{2s}\cdot\mathbf{g}')^{1/2}}. \tag{2.13}$$

These equations can be solved symbolically with the help of the resolvent operator,

$$a_{\mathbf{g}}^{(\alpha)}=\sum_{\mathbf{g}'\neq 0}\left(\frac{1}{s-\hat{\Gamma}}\right)_{\mathbf{g}\mathbf{g}'}r_{\mathbf{g}'}^{(\alpha)}\Bigg|_{s=1}, \tag{2.14}$$

where the parameter s has been introduced in order to facilitate the subsequent discussion. This formal solution is expanded in powers of $\hat{\Gamma}/s$,

$$a_{\mathbf{g}}^{(\alpha)}=\sum_{r=1}^{\infty}\frac{1}{s^r}\sum_{\mathbf{g}'\neq 0}(\hat{\Gamma}^{r-1})_{\mathbf{g}\mathbf{g}'}r_{\mathbf{g}'}^{(\alpha)}\Bigg|_{s=1}, \tag{2.15}$$

and this is used to calculate $\psi^{(\alpha)}(\mathbf{r})$ and the associated local electric field $\mathbf{E}^{(\alpha)}(\mathbf{r})$ and current density $\mathbf{J}^{(\alpha)}(\mathbf{r})$. This kind of power series is also used to calculate the bulk effective conductivity tensor $\hat{\sigma}_e$, defined by

$$\langle J_\alpha^{(\beta)}(\mathbf{r})\rangle\equiv\sigma_{\alpha\gamma}^{(e)}\langle E_\gamma^{(\beta)}(\mathbf{r})\rangle. \tag{2.16}$$

This is a much more efficient procedure than attempting to directly solve (2.11) using a truncated version of the matrix $\hat{\Gamma}$, because often a very large number of Fourier components need to be included in order to get results of acceptable accuracy (see Ref. 40).

C. Summary of previous results

The bulk effective conductivity tensor $\hat{\sigma}_e$, obtained using the procedure described in the previous subsection, enables us to calculate the bulk effective resistivity tensor $\hat{\rho}^{(e)}\equiv(\hat{\sigma}_e)^{-1}$. For an isolated spherical inclusion, there is one longitudinal element $\rho_\parallel^{(e)}$ and two identical transverse elements $\rho_\perp^{(e)}$ of Ohmic resistivity (i.e., diagonal elements of $\hat{\rho}^{(e)}$). These components of $\hat{\rho}^{(e)}$ are independent of the direction of **H**. Moreover, the off-diagonal elements of $\hat{\rho}^{(e)}$ are purely antisymmetric. However, even in the case of a simple cubic array of spherical inclusions, or a square array of cylindrical inclusions, the situation is much more complicated, unless **H** is along a principal symmetry axis, like (100). Otherwise, not only are the three diagonal elements of $\hat{\rho}^{(e)}$ usually different from each other, but the symmetric part of $\hat{\rho}^{(e)}$ will include off-diagonal elements too. We will always take **H** to lie in the plane defined by the (010) and (001) axes (the y,z plane), and focus attention on the diagonal elements of $\hat{\rho}^{(e)}$, defined by the direction of the volume averaged current density $\langle\mathbf{J}\rangle$ (see Fig. 2):

$$\rho_\parallel^{(e)} \quad \text{for } \langle\mathbf{J}\rangle\|\mathbf{H}\perp\mathbf{e}_x,$$

$$\rho_\perp^{(e)} \quad \text{for } \langle\mathbf{J}\rangle\|\mathbf{e}_x\|(100)\perp\mathbf{H}, \tag{2.17}$$

$$\rho\tilde{}_\perp^{(e)} \quad \text{for } \langle\mathbf{J}\rangle\|(\mathbf{e}_x\times\mathbf{H})\in y,z \text{ plane.}$$

In practice, we always calculate components of $\hat{\rho}^{(e)}$ along the principal symmetry axes. Therefore $\tilde{\rho}_\perp^{(e)}$ and $\rho_\parallel^{(e)}$ have to be calculated by applying to these components the appropriate rotation transformation $\hat{T}(\xi)$ by an angle ξ in the y,z-plane [see Fig. 2(b)]

$$\hat{T}(\xi)\hat{\rho}^{(e)}\hat{T}^{-1}(\xi), \tag{2.18}$$

where

$$\hat{T}(\xi)=\begin{pmatrix}1&0&0\\0&\cos\xi&-\sin\xi\\0&\sin\xi&\cos\xi\end{pmatrix}. \tag{2.19}$$

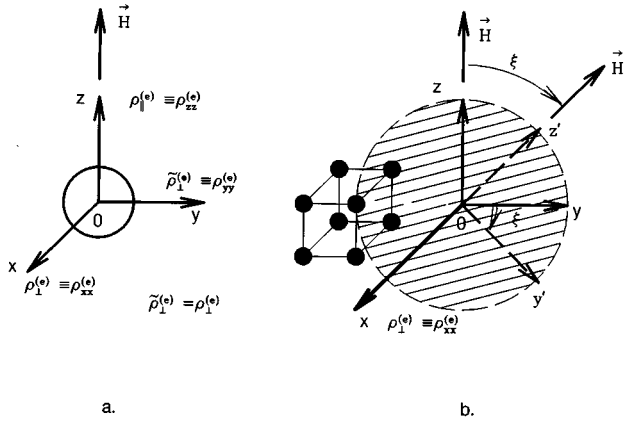

FIG. 2. Pictorial representation of the scheme used to calculate the various magnetoresistivity tensor components. The coordinate axes x,y,z always lie along the principal axes of a simple cubic lattice. The magnetic field $\mathbf{H}$ is always in the y,z plane and defines a rotated pair of coordinate axes y',z' in that plane, which make an angle ξ with the fixed y,z axes. The transverse resistivity component $\rho_{\perp}^{(e)} \equiv \rho_{xx}^{(e)}$ is calculated by making the volume averaged current density $\langle \mathbf{J} \rangle$ flow along the fixed x axis, which is always perpendicular to $\mathbf{H}$. The longitudinal component $\rho_{\parallel}^{(e)}$ is calculated by having $\langle \mathbf{J} \rangle$ parallel to $\mathbf{H}$, which rotates in the y,z plane. The second transverse component $\tilde{\rho}_{\perp}^{(e)}$ is calculated by taking $\langle \mathbf{J} \rangle$ in the y,z plane but perpendicular to $\mathbf{H}$; thus the direction of $\langle \mathbf{J} \rangle$ changes with the rotation of $\mathbf{H}$ in that plane. Note that $\rho_{\parallel}^{(e)}$ always differs from the other two components. $\rho_{\perp}^{(e)}$ and $\tilde{\rho}_{\perp}^{(e)}$ are also usually different. They only coincide when $\langle \mathbf{J} \rangle$ lies along either the y or the z axis, or when one is dealing with an isolated spherical inclusion. The numerical calculation always yields components of $\hat{\rho}^{(e)}$ along the fixed axes x,y,z; therefore, $\rho_{\parallel}^{(e)}$ and $\tilde{\rho}_{\perp}^{(e)}$ usually have to be calculated by invoking the coordinate transformation $y,z \rightarrow y',z'$.

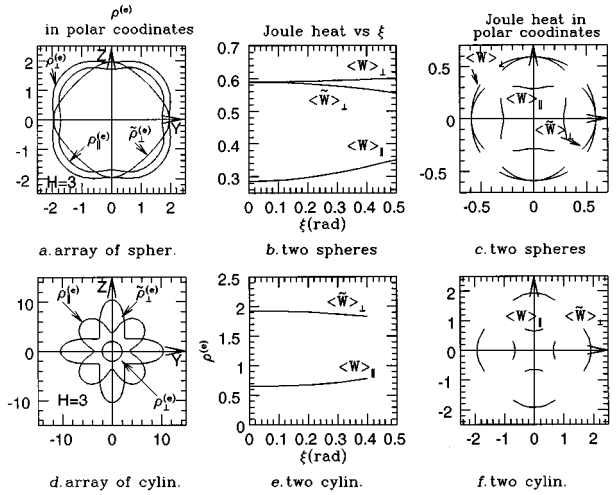

FIG. 3. (a)–(c) *Spherical inclusions*. (a) Plots of the absolute magnetoresistance components $\rho_{\perp}^{(e)}$, $\rho_{\parallel}^{(e)}$, and $\tilde{\rho}_{\perp}^{(e)}$ of a periodic composite with a cubic array of insulating spheres of radius $R=0.4$ and lattice constant 1, embedded in a free-electron host medium (after Ref. 1). (b) Longitudinal and transverse dissipation rates for a two sphere system, averaged over a square at the center of the symmetry plane between the spheres (see Fig. 9). The incident current density $\mathbf{J}_0$ is taken along three different directions, which correspond to $\rho_{\perp}^{(e)}$, $\rho_{\parallel}^{(e)}$, and $\tilde{\rho}_{\perp}^{(e)}$. (c) The same as (b) but plotted in polar coordinates, as in (a). (d)–(f) *Cylindrical inclusions*. (d) Plots of the absolute magnetoresistance components $\rho_{\parallel}^{(e)}$ and $\tilde{\rho}_{\perp}^{(e)}$ of a periodic composite with a square array of infinitely long insulating cylinders of radius $R=0.4$ and lattice constant 1, embedded in a free-electron host medium (after Ref. 1). (e) The analogue of (b) for a pair of parallel cylinders (see Fig. 9). (f) The same as (e) but plotted in polar coordinates, as in (d).

As an example, in Figs. 3(a) and 3(d) we show results, reproduced from Ref. 1, for the three diagonal elements $\rho_{\perp}^{(e)}$, $\tilde{\rho}_{\perp}^{(e)}$, and $\rho_{\parallel}^{(e)}$ in the case of a simple cubic array of insulating spherical obstacles and a square array of infinitely long insulating cylindrical obstacles. The distance from the origin in these plots gives the magnitudes of those resistivities as a function of the direction of $\mathbf{H}$ when its magnitude H is constant. For large enough H a strong anisotropy develops, and the variations with the direction of $\mathbf{H}$ become more pronounced with increasing H. Minima in the angular profiles of $\rho_{\perp}^{(e)}$ and $\rho_{\parallel}^{(e)}$ occur in the directions of the main crystallographic axes [see Fig. 3(a); in Fig. 3(d), $\rho_{\perp}^{(e)}$ is completely isotropic and field independent—that is due to the 2D nature of the parallel cylinders microgeometry[1]]. For similar systems, but with smaller inclusions, additional minima appear along other, low order crystallographic directions (see Ref. 1). This behavior can be understood using a simple geometric shadow picture of the interaction between current distortions caused by neighboring obstacles: The region of current distortion around each obstacle keeps increasing in length with H, and with it also the extra dissipation, as long as it does not encounter other obstacles. When the closest obstacle is encountered in the direction of $\mathbf{H}$, the current distortion begins to saturate and along with it the extra dissipation. Obviously, the magnitude of $\mathbf{H}$ at which this saturation occurs will fluctuate with the direction of $\mathbf{H}$, with minima appearing along low order crystal symmetry axes if H is large enough and if the obstacles are small enough.[1]

For other components of $\hat{\rho}^{(e)}$ this simple picture was not sufficient to explain the behavior found from numerical calculations. Thus, a simple geometrical shadow analysis could not explain why $\tilde{\rho}_{\perp}^{(e)}$ exhibits maxima (minima) in the same directions where $\rho_{\perp}^{(e)}$ had its minima (maxima).[1] In the following sections, we show that a more detailed analysis of the current distortion patterns around isolated obstacles and their mutual interactions is in fact able to account for all the important details of the observed phenomenology.

III. DISTRIBUTION OF THE LOCAL RATE OF DISSIPATION

The presence of both a strong magnetic field and a lattice of periodically arranged inclusions usually removes the degeneracy of the transverse components $\rho_{\perp}^{(e)}$, $\tilde{\rho}_{\perp}^{(e)}$, since these components now correspond to nonequivalent directions of $\langle \mathbf{J} \rangle$: In the case of $\rho_{\perp}^{(e)}$, $\langle \mathbf{J} \rangle$ lies along a fixed main crystallographic axis [the (100) or x axis], while in the case of $\tilde{\rho}_{\perp}^{(e)}$, $\langle \mathbf{J} \rangle$ lies along a changing direction in the y,z plane, which in general is not a symmetry axis. In this section we

describe the results of numerical calculations of the local rate of dissipation around an isolated spherical obstacle and around a simple cubic array of such obstacles.

From (2.18), (2.19) we get the following expressions for the components $\rho_{\parallel}^{(e)}$, $\tilde{\rho}_{\perp}^{(e)}$ in the case where **H** lies in the y,z plane, making an angle ξ with the y axis [see Fig. 2(b)]:

$$\tilde{\rho}_{\perp}^{(e)}(\xi)=\rho_{yy}^{(e)}(\xi)\cos^2\xi+\rho_{zz}^{(e)}(\xi)\sin^2\xi-\tfrac{1}{2}[\rho_{yz}^{(e)}(\xi)+\rho_{zy}^{(e)}(\xi)]\sin 2\xi, \tag{3.1}$$

$$\rho_{\parallel}^{(e)}(\xi)=\rho_{zz}^{(e)}(\xi)\cos^2\xi+\rho_{yy}^{(e)}(\xi)\sin^2\xi+\tfrac{1}{2}[\rho_{yz}^{(e)}(\xi)+\rho_{zy}^{(e)}(\xi)]\sin 2\xi. \tag{3.2}$$

For small ξ these expressions can be expanded to order ξ^2, yielding

$$\tilde{\rho}_{\perp}^{(e)}(\xi)\approx\rho_{yy}^{(e)}(0)-\{[\rho_{yy}^{(e)}(0)-\rho_{zz}^{(e)}(0)]+[\rho_{yz}^{(e)\prime}(0)+\rho_{zy}^{(e)\prime}(0)]-\tfrac{1}{2}\rho_{yy}^{(e)\prime\prime}(0)\}\xi^2, \tag{3.3}$$

$$\rho_{\parallel}^{(e)}(\xi)\approx\rho_{zz}^{(e)}(0)+\{[\rho_{yy}^{(e)}(0)-\rho_{zz}^{(e)}(0)]+[\rho_{yz}^{(e)\prime}(0)+\rho_{zy}^{(e)\prime}(0)]+\tfrac{1}{2}\rho_{zz}^{(e)\prime\prime}(0)\}\xi^2, \tag{3.4}$$

where the primes signify derivatives. In both of these expressions, all three terms which appear inside the curly brackets are positive. This is found from the numerical calculations for all values of H. We conclude that $\tilde{\rho}_{\perp}^{(e)}$ has a maximum at $\xi=0$, while $\rho_{\parallel}^{(e)}$ has a minimum there, in agreement with Figs. 3(a), 3(d).

We turn to consider the local rate of dissipation, given by $W(\mathbf{r})=\mathbf{J}(\mathbf{r})\cdot\mathbf{E}(\mathbf{r})$. When this quantity is averaged over the entire volume for a given value of $\langle\mathbf{J}\rangle$, the result is proportional to the diagonal component of $\hat{\rho}^{(e)}$ along the direction of $\langle\mathbf{J}\rangle$.

We start by considering a single inclusion and writing the local current density $\mathbf{J}(\mathbf{r})$ as

$$\mathbf{J}(\mathbf{r})=\mathbf{J}_0+\delta\mathbf{J}(\mathbf{r}), \tag{3.5}$$

where $\mathbf{J}_0$ is the current injected far away from the inclusion and $\delta\mathbf{J}(\mathbf{r})$ is the distortion produced by the inclusion. In the absence of a magnetic field, the distortion has a simple dipolar shape. When a strong magnetic field **H** is present, the distortion has a more complicated shape, but for a perfectly insulating inclusion of either spherical or cylindrical shape, this problem was solved exactly some years ago.[39]

In Fig. 4 we show 3D plots of $W(x,y,z_0)$, calculated in the planes $z_0=0.3$, $z_0=0.6$ for an insulating spherical inclusion of radius $R=0.2$, located at the origin and subject to a magnetic field $H=10$ (in dimensionless units) along the z axis. Plots are shown for the longitudinal case $\mathbf{J}_0\|\mathbf{H}\|z$ [Figs. 4(a) and 4(c)] and the transverse case $\mathbf{J}_0\|x\perp\mathbf{H}$ [Figs. 4(b) and 4(d)]. In the longitudinal case the dissipation has azimuthal symmetry and is peaked at a circle roughly equal to the projection of the obstacle. When z_0 is increased the radius of this circle decreases [see Fig. 5(a)], as do the height and sharpness of the dissipation peak [compare Figs. 4(a) and 4(c)], until for $z_0>HR$ the extra dissipation above the uniform background becomes negligible. In the transverse case, by contrast, W does not have azimuthal symmetry. Instead, it exhibits a pair of maxima and a pair of minima at four points which also lie on the above mentioned circle [see Figs. 4(b) and 4(d)]. This also appears in Fig. 6, which shows a sequence of topographic contour plots of $W(x,y,z_0)$ for that case at different values of H. In those plots, lighter shades of gray correspond to larger values of W. Similarly to the longitudinal case, it seems that the lateral positions of the four extremum points tend to the origin in the z_0 plane with increasing z_0 [see Fig. 5(b)], and their height (depth) deteriorates and quickly becomes negligible when $z_0>HR$ [com-

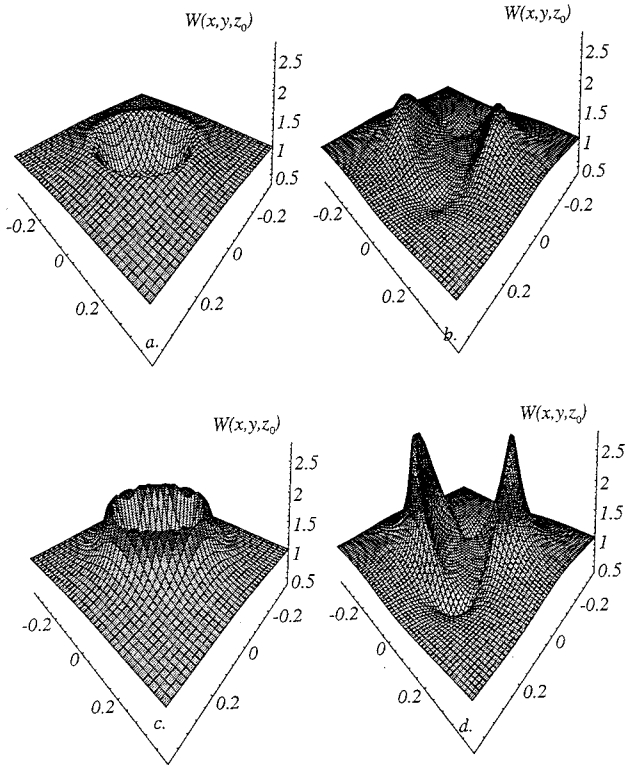

FIG. 4. 3D plots of the power dissipation function $W(x,y,z_0)$, calculated for fixed z_0 as a function of x,y near a *single* spherical obstacle of radius $R=0.2$, with $\mathbf{H}\|z$ and $H=10$ and (a) $z_0=0.6$ and $\mathbf{J}_0\|\mathbf{H}\|z$ (longitudinal case), (b) $z_0=0.6$ and $\mathbf{J}_0\|x\perp\mathbf{H}$ (transverse case), (c) $z_0=0.3$ and $\mathbf{J}_0\|\mathbf{H}\|z$, (d) $z_0=0.3$ and $\mathbf{J}_0\|x\perp\mathbf{H}$. In the longitudinal case the maxima of $W(x,y,z_0)$ define a quasiconical surface with the cone axis parallel to **H**, while in the transverse case they define a pair of lines along such a surface. In the latter case there are actually two maxima and two minima in every constant z_0 plane. When that plane is taken further away from the sphere, both the height and the sharpness of the dissipation extrema become less pronounced, until for $z_0>HR$ the extra dissipation above the uniform background value becomes negligible.

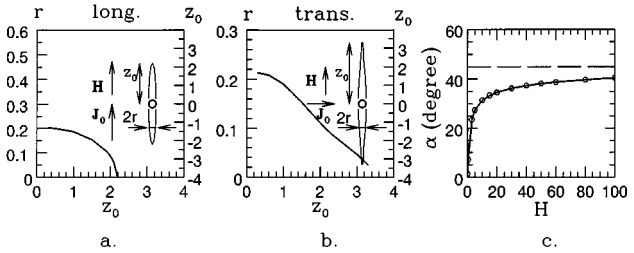

FIG. 5. (a) The radius r of the circular ridge of maxima [see Fig. 4(c)] vs z_0 for the longitudinal case when $H=10$. (b) One-half of the distance between the two maxima (or between the two minima) of Figs. 4(d) and 6 vs z_0 for the transverse case, when $H=10$. The locations of the maxima with respect to the size of the obstacle and their dependence on z_0 is depicted on the right sides (together with the scale for z_0) of two graphs (a) and (b). (c) The inclination angle α of the two maxima (or minima) of Fig. 6 plotted vs H. The magnitude of this angle tends to $\pi/4$ as $H\to\infty$.

pare Figs. 4(b) and 4(d)]. The positions of the two maxima on the circumference of the circle define an inclination angle α with respect to the y axis. This angle, as well as the existence and height of the maxima, depends on the magnitude of H, with $\alpha\to\pi/4$ as $H\to\infty$ [see Figs. 6 and 5(c)].

In order to produce similar plots for W in the case of a simple cubic array of insulating spherical inclusions, we used the numerical methods described in the previous section. Figure 7 shows topographic contour plots of $W(x,y,z_0)$ for a sequence of values of H, taken at $z_0=0.35$, while the sphere radius is $R=0.3$ and the lattice constant is 1. The magnetic field is along the z axis, perpendicular to the plane of the figure, while the average current density $\langle\mathbf{J}\rangle$ is along

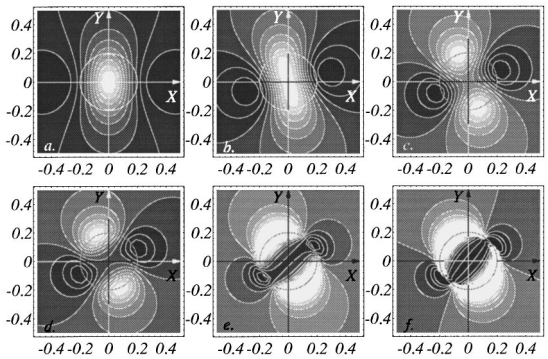

FIG. 6. Contour plots of the power dissipation function $W(x,y,z_0)$, $z_0=0.3$, for a single spherical obstacle of radius $R=0.2$, with an imposed transverse magnetic field. (a)–(f) show the evolution of the dissipation pattern with increasing H in the following sequence: 0,1,2,3,10,100. The gray scale is not the same in the different plots: The shade changes by equal steps from black (which corresponds to the minimal value, $W_{\min}$) to white (which corresponds to the maximal value, $W_{\max}$). The absolute values of $W(x,y,z)$ in each figure can be inferred from the the extremum values: (a) $W_{\max}=1.574$, $W_{\min}=0.963$; (b) $W_{\max}=1.239$, $W_{\min}=0.890$; (c) $W_{\max}=1.313$, $W_{\min}=0.788$; (d) $W_{\max}=1.480$, $W_{\min}=0.703$; (e) $W_{\max}=2.91$, $W_{\min}=0.57$; (f) $W_{\max}=21.550$, $W_{\min}=0.150$. The lateral position of the obstacle is shown as a circle at the center of each plot. A uniform current density $\mathbf{J}_0\|x$ is injected uniformly at $x=-\infty$, while $\mathbf{H}\|z$ (i.e., perpendicular to the plane of the figure).

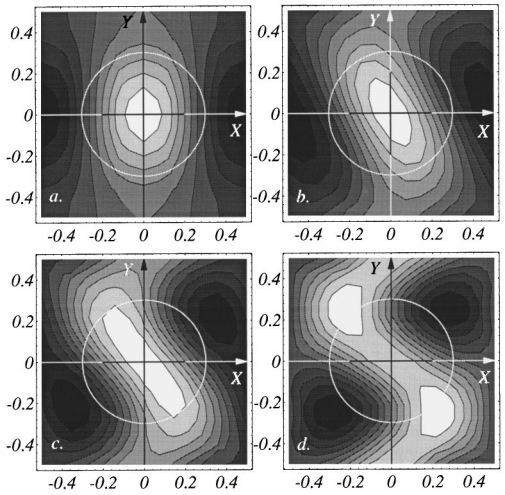

FIG. 7. Evolution of the dissipation pattern with increasing H for a *simple cubic array of spherical obstacles* of radius $R=0.3$ in the case $\langle\mathbf{J}\rangle\|x\perp\mathbf{H}\|z$. Shown are contour plots of $W(x,y,z_0)$ for fixed $z_0=0.35$, where $x=y=z=0$ corresponds to a sphere center. The values of H used in (a)–(d) are 0,1,1.7, and 3, respectively. The gray scales are similar to those of Fig. 6. The maximal and minimal values of $W(x,y,z_0)$, which can be used to infer the absolute scale, are (a) $W_{\max}=1.574$, $W_{\min}=0.556$; (b) $W_{\max}=0.783$, $W_{\min}=0.495$; (c) $W_{\max}=0.408$, $W_{\min}=0.161$; (d) $W_{\max}=0.180$, $W_{\min}=0.049$. The lateral position of the sphere at the origin, which lies below the plane of the figure, is shown as a circle at the center of each plot. In order to avoid an excessively lengthy numerical computation, a much smaller number of Fourier components were used in this calculation (i.e., from -1 to 1 along each axis in reciprocal space) than in calculations of $\hat{\sigma}_e$.

the (100) direction or x axis. These plots are evidently similar to the ones shown in Fig. 6 for a single sphere, but they exhibit the expected square symmetry. In Fig. 8 we show similar plots at the fixed value $H=3$ for two different sphere radii, and for $\langle\mathbf{J}\rangle\|x$ (transverse) as well as for $\langle\mathbf{J}\rangle\|z$ (longitudinal). As expected, when R increases, the deviations of W from the isolated inclusion form also increase: In the transverse case an additional peak or ''hot spot'' appears at $x=y=0$, directly over the center of the inclusion [Figs. 8(a), 8(c)]. In the longitudinal case, four subsidiary peaks appear on the x,y axes at small R, then shift to locations on the two diagonals $x=\pm y$ when R increases [Figs. 8(b), 8(d)].

In summary, it is obvious that, if the spheres are not too large, the deviations from isolated sphere behavior will be small. However, due to the complex nature of the current distortions even around an isolated sphere, the interactions between the distortion effects of different inclusions can be quite subtle. The simple geometric shadow picture which was used earlier cannot be expected to explain those subtleties. In the next section we attempt to understand some of these subtleties, and their effects on macroscopic behavior, by considering the *interference* between distortions produced by just two obstacles.

IV. TWO OBSTACLE INTERFERENCES

In principle, we wish to approximate the current density $\mathbf{J}(\mathbf{r})$ as

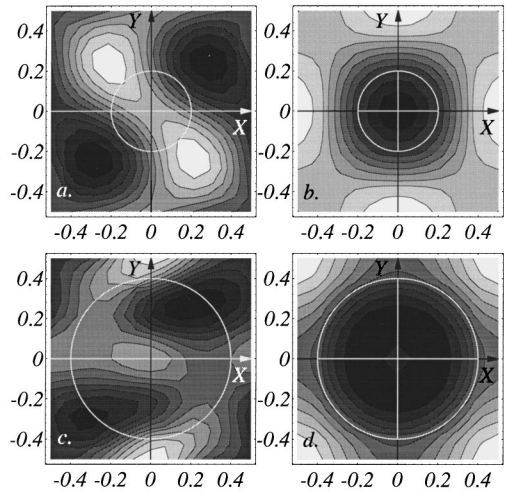

FIG. 8. (a) and (b) Contour plots of the dissipation function $W(x,y,z_0)$, $z_0=0.3$ for the same periodic composite as in Fig. 7, with $\langle \mathbf{J}\rangle \| x \perp \mathbf{H} \| z$, $\langle \mathbf{J}\rangle \| \mathbf{H} \| z$, respectively, and with $H=3$. These calculations would correspond to $\rho_{\perp}^{(e)}$ [(a)], $\rho_{\|}^{(e)}$ [(b)]. (c), (d) The same as (a), (b), but with a larger sphere radius $R=0.4$ and $z_0=0.45$. The maximal and minimal values of $W(x,y,z_0)$, which can be used to infer the absolute gray scale, are (a) $W_{\max}=0.132$, $W_{\min}=0.074$; (b) $W_{\max}=1.058$, $W_{\min}=0.746$; (c) $W_{\max}=0.308$, $W_{\min}=0.042$, (d) $W_{\max}=1.054$, $W_{\min}=0.318$.

$$\mathbf{J}(\mathbf{r}) \cong \langle \mathbf{J}\rangle + \sum_n \delta\mathbf{J}(\mathbf{r}-\mathbf{R}_n), \tag{4.1}$$

where $\delta\mathbf{J}(\mathbf{r})$ is the current distortion caused by an isolated sphere at $r=0$. As shown in the previous section, this is a reasonable approximation if H is not too large and if R is small. Because we intend to use this approximation only for gaining a better *qualitative* understanding of the behavior of $\hat{\rho}^{(e)}$, we limit our considerations to a pair of spheres (or cylinders), focusing attention on $\mathbf{J}(\mathbf{r})$ and $W(\mathbf{r})$ in a square

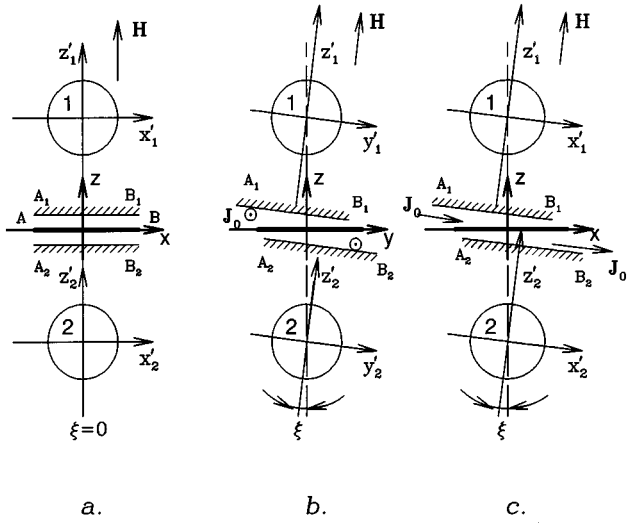

FIG. 9. Illustration of the obstacle pair interference calculation as a function of the inclinations of $\mathbf{H}$, $\mathbf{J}_0$. In (b) and (c), $\mathbf{J}_0$ is shown to lie along the x axis, but the illustration can also be used to discuss the case where $\mathbf{J}_0 \| z$.

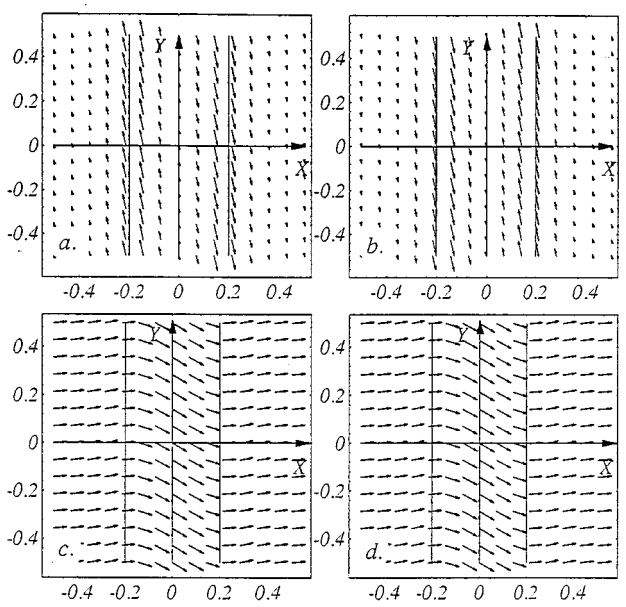

FIG. 10. Vector field plots of the current distortions calculated for two infinitely long cylinders (see Fig. 9) in the longitudinal [(a), (b)] and transverse [(c), (d)] cases. Vector plots of the x,y plane components of current distortion produced by the upper cylinder [see the A_1B_1 plane in Fig. 9(a)] are shown in (a) and (c), while the analogous fields produced by the lower cylinder [see the A_2B_2 plane in Fig. 9(a) are shown in (b) and (d). In all cases $\mathbf{H} \| z$ and $H=10$. The lateral location of the cylinders of radius $R=0.2$ is indicated by two vertical lines.

that is situated symmetrically between them and is perpendicular to the z axis which connects their centers (see Fig. 9). The field $\mathbf{H}$ lies along that axis, while a uniform current density $\mathbf{J}_0$ is injected far away along either the x axis (transverse) or the z axis (longitudinal). Figure 9(a) shows a projection onto the x,z plane of the two spheres/cylinders and the above mentioned square, denoted by the thick line segment which we call AB. Also shown are the two squares A_1B_1, A_2B_2, where the current distortions from the two isolated spheres must be superposed in order to obtain $\mathbf{J}(\mathbf{r})$. Those squares coincide with AB when $\mathbf{H} \| z$ *exactly*, but are shifted as shown in Figs. 9(b) and 9(c) when $\mathbf{H}$ is tilted away from that direction. Figure 10 shows 2D vector plots of the x,y components of $\mathbf{J}_i(\mathbf{r})$ in those squares for $i=1$ (upper cylinder—left hand plots) and $i=2$ (lower cylinder—right hand plots). The plots for the transverse case appear at the bottom, those for the longitudinal case appear at the top. In the longitudinal case it is clear that the exhibited x,y components of $\mathbf{J}_i(\mathbf{r})$ will cancel each other when the squares A_1B_1, A_2B_2 are superposed without any shifts, but will not cancel when the two squares are shifted sideways, as in Fig. 9(c). Unless overwhelmed by different behavior of the z component, this behavior should lead to a minimum of $\rho_{\|}^{(e)}$ when $\mathbf{H}$ is in the z direction. Similarly, it is clear that in the transverse case, the exhibited x,y components of $\mathbf{J}_i(\mathbf{r})$ will add coherently when the squares A_1B_1, A_2B_2 are superposed without any shifts, but will tend to cancel when the two squares are shifted sideways, as in Fig. 9(c). Thus, with the same qualifications regarding the behavior of the z component, we can expect that $\tilde{\rho}_{\perp}^{(e)}$ will have a maximum when $\mathbf{H}$

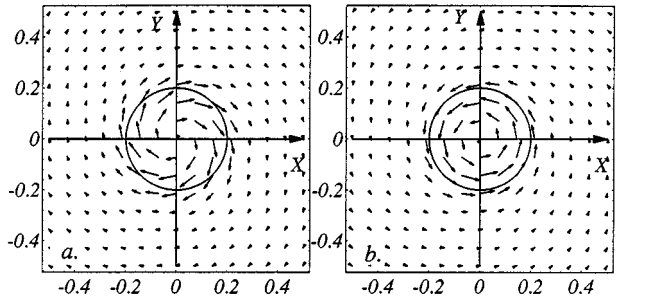

FIG. 11. Vector field plot of the x,y current components produced by two spheres in the plane of symmetry between them (see Fig. 9) in the *longitudinal* case. The current distortions produced by the upper sphere (a) exhibit a clockwise sense of circulation while the distortions produced by the lower sphere (b) circulate in the opposite sense. The magnetic field is $H=5$, the sphere radius is $R=0.2$, and the distance between the centers is 1. The lateral position of the spheres is indicated by a circle.

is in the z direction. In fact, the behavior of the z components, although opposite to the behavior of the x,y components, does not change the conclusions reached above.

In order to give a similar discussion for the case of two spherical obstacles, we show in Fig. 11 vector plots of the x,y components of $\mathbf{J}$ on the two squares A_1B_1, A_2B_2, as produced by each sphere individually when $\mathbf{H}\|z$. Figures 11(a) and 11(b) show the current fields produced by the upper and lower spheres, respectively, when $\mathbf{J}_0\|z$ (longitudinal case). Clearly, when the two fields are superimposed without any shifts, then the currents cancel perfectly, whereas when they are superimposed with a shift, there is less cancellation. Consequently, if the behavior of the J_z component does not overwhelm this behavior, we expect that $\rho_{\|}^{(e)}$ will have a minimum when $\mathbf{H}$ lies along the z axis. In order to study the interference effects when $\mathbf{J}_0\|x$ (transverse case), we show in Fig. 12 topographic contour plots of all three components of current distortions δJ_{ix}, δJ_{iy}, δJ_{iz} for the two spheres $i=1,2$ on the same two squares A_1B_1, A_2B_2. The gray shade coding is now such that white denotes the *maximum positive deviation* with respect to background while black denotes the *maximum negative deviation* with respect to background. It is now evident that while the x and y components add coherently, the z components cancel when there is no shift, i.e., when $\mathbf{H}\|z$. Then, when $\mathbf{H}$ is tilted away from the z axis, the degree of cancellation of δJ_{iz} is always decreased, as is the degree of coherence of δJ_{ix}, δJ_{iy}. When the tilt, and hence also the relative shift of the vector plots, is along the y axis, the dominant effect is an increase of $\delta J_{1z}+\delta J_{2z}$—this explains the minimum of $\rho_{\perp}^{(e)}$ when $\mathbf{H}\|z$. By contrast, when the tilt and the shift are along the x axis, the dominant effect is the decrease of $\delta J_{1y}+\delta J_{2y}$—this explains the maximum of $\tilde{\rho}_{\perp}^{(e)}$ when $\mathbf{H}\|z$. In this connection we note that the large contribution $2[J_0(\delta J_{1x}+\delta J_{2x})]$, which appears in the local dissipation rate W and is linear in δJ_{ix}, *vanishes* when integrated over x, y. Therefore only the quadratic contributions were included in the above considerations.

In order to confirm these qualitative arguments, we also used the two obstacle system to calculate an approximation

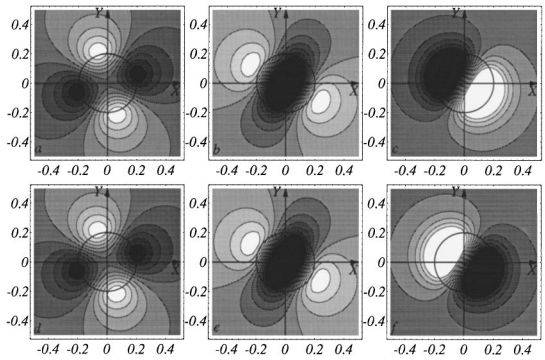

FIG. 12. Contour plots of the three components of current distortions $\delta J_{ix}(x,y,z_0)$, $\delta J_{iy}(x,y,z_0)$, and $\delta J_{iz}(x,y,z_0)$, produced by the upper sphere $i=1$ [(a), (b), and (c)] and the lower sphere $i=2$ [(d), (e), and (f)] in a two obstacle configuration (see Fig. 9), when $\mathbf{H}$ lies along the z axis which passes through the sphere centers. Positive values are shown as light shades and negative values as dark shades. The extra power dissipation due to the distortion $|\mathbf{J}_0+\delta\mathbf{J}_1(x,y,z_0)+\delta\mathbf{J}_2(x,y,z_0)|^2-|\mathbf{J}_0|^2$, when integrated over x and y, is entirely determined by $|\delta\mathbf{J}_1(x,y,z_0)+\delta\mathbf{J}_2(x,y,z_0)|^2$, since the linear terms in δJ_{ix} vanish upon integration. What happens when the direction of $\mathbf{H}$ is changed can be described by shifting the contour plots produced by the two spheres with respect to each other before superposing them and squaring. The magnetic field is $H=2$, the sphere radius is $R=0.2$, and the distance between the centers is 1.

for the total dissipation rate by using the superposition approximation to calculate the local dissipation rate $\mathbf{J}\cdot\mathbf{E}$ and then integrating this function over the square AB. The results of this calculation for the two-sphere system are shown in Figs. 3(b), 3(c)—they clearly confirm our expectations and are qualitatively similar to the more exact numerical results for a simple cubic array of spheres shown in Fig. 3(a). A similar calculation was also performed for the two-cylinder system—the results are shown in Figs. 3(e), 3(f), along with results of numerical calculations on a square array of cylinders in Fig. 3(d); the conclusions are similar.

V. DISCUSSION AND SUMMARY

We studied the strong dependence of the bulk effective magnetoresistivity tensor $\hat{\rho}^{(e)}(\mathbf{H})$ of a periodic composite medium on the direction of $\mathbf{H}$ for strong fields. This was done with the help of detailed plots of the local current density field and the local rate of dissipation around a single, isolated inclusion, as well as plots of the local dissipation rate produced by a periodic array of inclusions. The strong angular variations of the components of $\hat{\rho}^{(e)}$ are due to interactions between the current distortions produced by different inclusions. Although some features of the angular dependence of the resistivity components $\rho_{\perp}^{(e)}$, $\rho_{\|}^{(e)}$ can be understood by invoking a simple geometrical shadow picture of that interaction, other features, and the behavior of other components of $\hat{\rho}^{(e)}$, can only be explained by a detailed consideration of the interference between distortions produced by neighboring inclusions. By considering this interference in the case where there are only two inclusions, we were able to explain why $\tilde{\rho}_{\perp}^{(e)}$ exhibits a maximum when $\mathbf{H}$

lies along the (100) axis, while both $\rho_{\perp}^{(e)}$ and $\rho_{\parallel}^{(e)}$ have a minimum there.

The anisotropies which are found in calculations of the magnetoresistance of periodic composites bear remarkable similarities to the anisotropies that are observed in the magnetoresistance of single crystals of transition metals at low temperatures, but their origin is quite different. In the case of a composite medium this is an entirely classical phenomenon: quantum mechanics plays no role. This is in contrast with the situation in transition metal crystals, where the detailed structure of the Fermi surface, which must be noncompact, is responsible for the strong anisotropies. Since the model of a classical composite medium is not a reasonable approximation for a metallic crystal, measurements of $\hat{\rho}^{(e)}$ on such crystals are irrelevant for comparison with our calculations. For that purpose, it would be necessary to fabricate a periodic conducting composite in which quantum effects are negligible. That means a composite where all the relevant microscopic lengths, like mean free path and de Broglie wavelengths of the charge carriers, are small compared to the inhomogeneity length scale or the sizes of the inclusions. According to calculations published elsewhere, a strongly anisotropic magnetoresistance will appear not only in composites with a three-dimensional periodic microstructure, but also in two-dimensional periodic microstructures, and even when the system is a thin film.[35] The latter class of materials should be easier to fabricate. It may also be worthwhile to extend the classical model by including quantum corrections as a small perturbation: Under certain conditions, such an approach might be relevant for a periodic mesoscopic array of quantum dots.

ACKNOWLEDGMENTS

This research was supported in part by grants from the U.S.-Israel Binational Science Foundation and the Israel Science Foundation.

[1] D. J. Bergman and Y. M. Strelniker, Phys. Rev. B **49**, 16 256 (1994).
[2] U. Dai, A. Palevski, and G. Deutscher, Phys. Rev. B **36**, 790 (1987).
[3] M. Rhode and H. Micklitz, Phys. Rev. B **36**, 7289 (1987).
[4] H. Stachowiak, Physica **45**, 481 (1970).
[5] D. Stroud, and F. P. Pan, Phys. Rev. B **13**, 1434 (1976).
[6] I. Webman, J. Jortner, and M.H. Cohen, Phys. Rev. B **15**, 1936 (1977).
[7] B. I. Shklovskii, Zh. Éksp. Teor. Fiz. **72**, 288 (1977) [Sov. Phys. JETP **45**, 152 (1977)].
[8] J. P. Straley, J. Phys. C **13**, 4335 (1980); **13**, L773 (1980).
[9] D. J. Bergman, Y. Kantor, D. Stroud, and I. Webman, Phys. Rev. Lett. **50**, 1512 (1983).
[10] D. J. Bergman, in *Percolation Structures and Processes*, edited by G. Deutscher, R. Zallen, and J. Adler, Annals of the Israel Physical Society Vol. 5 (Adam-Hilger, London, 1983), pp. 297–321.
[11] D. J. Bergman and D. Stroud, Phys. Rev. B **32**, 6097 (1985).
[12] D. J. Bergman, Philos. Mag. B **56**, 983 (1987).
[13] A. S. Skal, J. Phys. C **20**, 245 (1987).
[14] J. P. Straley, Phys. Rev. B **38**, 11 639 (1988).
[15] D. J. Bergman, E. Duering, and M. Murat, J. Stat. Phys. **58**, 1 (1990); still more references can be found in this article.
[16] A. K. Sarychev, D. J. Bergman, and Y. M. Strelniker, Europhys. Lett. **21**, 851 (1993).
[17] A. K. Sarychev, D. J. Bergman, and Y. M. Strelniker, Phys. Rev. B **48**, 3145 (1993).
[18] E. Yablonovich, T. J. Gmitter, and K. M. Leung, Phys. Rev. Lett. **67**, 2295 (1991).
[19] J. H. Evans, Nature (London) **229**, 403 (1971).
[20] J. H. Evans, Radiat. Eff. **10**, 55 (1971).
[21] B. A. Loomis, S. B. Gerber, and A. Taylor, J. Nucl. Mater. **68**, 19 (1977).
[22] K. Krishan, Radiat. Eff. **66**, 121 (1982).
[23] C. Tölg, M. Zaiser, P. Hähner, and W. Frank, Appl. Phys. A **58**, 3 (1994).
[24] D. Weiss, M. L. Roukes, A. Menschig, P. Grambow, K. von Klitzing, and G. Weimann, Phys. Rev. Lett. **66**, 2790 (1991).
[25] D. Weiss, K. Richter, A. Menshig, R. Bergmann, H. Schweizer, K. von Klitzing, and G. Weimann, Phys. Rev. Lett. **70**, 4118 (1993).
[26] W. Kang, H. L. Storner, L. N. Pfeiffer, K. W. Baldwin, and K.W. West, Phys. Rev. Lett. **71**, 3850 (1993).
[27] R. Shuster, G. Ernst, K. Ensslin, M. Entin, M. Holland, G. Böhm, and W. Klein, Phys. Rev. B **50**, 8090 (1994).
[28] D. Huang, G. Gumbs, and A. H. MacDonald, Phys. Rev. B **48**, 2843 (1993).
[29] V. G. Burnett, A. L. Efros, and F. G. Pikus, Phys. Rev. B **48**, 14 365 (1993).
[30] G. Chen, G. Klimeck, S. Datta, G. Chen, and W. A. Goddard III, Phys. Rev. B **50**, 8035 (1994).
[31] L. Bányai and S. W. Koch, *Semiconductor Quantum Dots* (World Scientific, Singapore, 1993).
[32] G. M. Sundaram, H. J. Bassom, R. J. Nicholas, G. J. Rees, P. J. Heard, P. D. Prewett, J. E. F. Frost, G. A. C. Jones, D. C. Peacock, and D. A. Ritchie, Phys. Rev. B **47**, 7348 (1993).
[33] G. Kirchenow, Phys. Rev. B **46**, 1439 (1992).
[34] K. Ensslin and P. M. Petroff, Phys. Rev. B **41**, 12 307 (1990).
[35] D. J. Bergman and Y. M. Strelniker, Phys. Rev. B **51**, 13 845 (1995).
[36] J. R. Klauder and J. E. Kunzler, in *The Fermi Surface*, edited by W. A. Harrison and M. B. Webb (John Wiley, New York, 1960), p. 125.
[37] R. G. Chambers, in *The Fermi Surface*, (Ref. 36), p. 100.
[38] I. M. Lifshits, M. Ya. Azbel, and M. I. Kaganov, *Electron Theory of Metals* (Consultants Bureau, New York, 1973).
[39] J. B. Sampsell and J. C. Garland, Phys. Rev. B **13**, 583 (1976).
[40] Y. M. Strelniker and D. J. Bergman, Phys. Rev. B **50**, 14 001 (1994).